Mon. Not. R. Astron. Soc. **386,** 807–818 (2008) doi:10.1111/j.1365-2966.2008.12980.x

The AzTEC mm-wavelength camera

G. W. Wilson,[1⋆] J. E. Austermann,[1] T. A. Perera,[1] K. S. Scott,[1] P. A. R. Ade,[2] J. J. Bock,[3] J. Glenn,[4] S. R. Golwala,[5] S. Kim,[6] Y. Kang,[6] D. Lydon,[1] P. D. Mauskopf,[2] C. R. Predmore,[7] C. M. Roberts,[1] K. Souccar[1] and M. S. Yun[1]

[1]*Department of Astronomy, University of Massachusetts, Amherst, MA 01003, USA*
[2]*Physics and Astronomy, Cardiff University, 5, The Parade, PO Box 913, Cardiff CF24 3YB*
[3]*Jet Propulsion Laboratory, California Institute of Technology, 4800 Oak Grove Drive, Pasadena, CA 91109, USA*
[4]*Center for Astrophysics and Space Astronomy, 389-UCB, University of Colorado, Boulder, CO 80309, USA*
[5]*California Institute of Technology, 1200 East California Boulevard, MC 59-33, Pasadena, CA 91125, USA*
[6]*Astronomy & Space Science Department, Sejong University, 98 Kwangjin-gu, Kunja-dong, 143-747, Seoul, South Korea*
[7]*Predmore Associates, South Deerfield, MA 01373, USA*

Accepted 2008 January 16. Received 2007 December 21; in original form 2007 October 29

ABSTRACT

AzTEC is a mm-wavelength bolometric camera utilizing 144 silicon nitride micromesh detectors. Here, we describe the AzTEC instrument architecture and its use as an astronomical instrument. We report on several performance metrics measured during a three-month observing campaign at the James Clerk Maxwell Telescope and conclude with our plans for AzTEC as a facility instrument on the Large Millimetre Telescope.

Key words: instrumentation: detectors – galaxies: high redshift – galaxies: starburst – submillimetre.

1 INTRODUCTION

In the era of the Atacama Large Millimeter Array (ALMA), the scientific niche for large mm-wave telescopes comes in the ability to use array receivers to make large surveys of the sky. The last decade has seen a series of major advances in mm-wavelength bolometric instruments, and it is now commonplace for ground-based telescopes to have mm/sub-mm wavelength cameras with tens to hundreds of detectors: for example, the Submillimetre Common-User Bolometer Array (SCUBA) on the James Clerk Maxwell Telescope (JCMT) (Holland et al. 1999); the Max Planck Millimeter Bolometer Array (MAMBO) on the Institut de Radio Astronomie Millimetrique (IRAM) 30-m telescope (Kreysa et al. 1998) and Bolocam on the Caltech Submillimetre Observatory (Glenn et al. 2003; Haig et al. 2004). AzTEC is a mm-wavelength bolometer camera designed for the Large Millimetre Telescope (LMT). Its 144 silicon nitride micromesh bolometers operate with a single bandpass centred at 1.1, 1.4, or 2.1 mm, with one bandpass available per observing run. AzTEC was commissioned at 1.1 mm during an engineering run at the JCMT in 2005 June and completed a successful observing run at the JCMT from 2005 November–2006 February during the JCMT05B semester. In 2007, the instrument was installed on the 10 m Atacama Submillimetre Telescope Experiment (ASTE) where it will work as a facility instrument through 2008. AzTEC will be installed on the LMT in early 2009.

In its 1.1-mm wavelength configuration, AzTEC is sensitive to the Rayleigh–Jeans tail of the thermal continuum emission from cold dust grains. Consequently, AzTEC is well-suited for extragalactic surveys of dusty, optically obscured starburst (or AGN-host) galaxies detected by their sub-mm/mm emission (so-called Sub-Millimetre Galaxies, or SMGs). As the far-infrared (FIR) peak of the cold dust emission is increasingly redshifted to mm-wavelengths with increasing distance, AzTEC is equally sensitive to dusty galaxies with redshift $z \geqslant 1$. The AzTEC/JCMT05B surveys of the Lockman Hole and the Subaru Deep Field (Austermann et al., in preparation), COSMOS (Scott et al. 2008) and GOODS-North (Perera et al., in preparation) represent the largest SMG surveys with uniform high sensitivity ($1\sigma \sim 1$ mJy) ever conducted, successfully demonstrating the superb mapping speed and stability of the instrument and providing a new insight on the clustering and cosmic variance of the SMG population. In a similar vein, AzTEC's high mapping speed and high sensitivity make it an interesting instrument for studies of cold dust in the Milky Way and in nearby galaxies.

Configured for 1.4- and 2.1-mm observations, AzTEC will be tuned to make high-resolution images of the Sunyaev–Zel'dovich effect in clusters of galaxies. AzTEC on the LMT will have a per-pixel resolution of 10 arcsec at 2.1 mm (5 arcsec at 1.1 mm) and will therefore be an unprecedented instrument for the study of the energetics of the free electron gas in clusters.

In this paper, we report on the design and performance of the AzTEC instrument. In Section 2, we describe the components of the instrument and its configuration. The observing software, mapping strategies and practical observing overheads are addressed in Section 3. We describe the calibration of AzTEC data in Section 4, and in Section 5 we list the sensitivity and mapping speeds of AzTEC as measured at the JCMT during the JCMT05B

⋆E-mail: wilson@astro.umass.edu

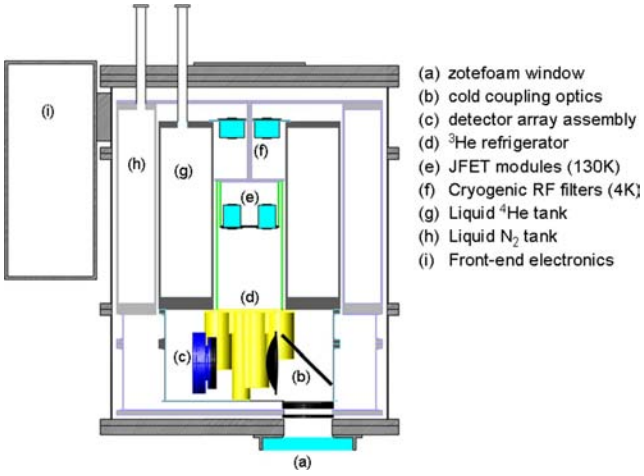

Figure 1. A cut-away view of the AzTEC cryostat. Mechanical supports have been removed for clarity.

run. We conclude with a brief discussion of the future of AzTEC in Section 6.

2 SYSTEM DESIGN

A cut-away view of the AzTEC instrument is shown in Fig. 1. Each subsystem labelled in the figure is described in detail below.

2.1 Cryostat and cryogenics

The AzTEC detector array is cooled using a three-stage, closed-cycle ^{3}He refrigerator (Bhatia et al. 2000) mounted to a liquid-cooled 4 K cryostat. Operation of the AzTEC refrigerator is fully automated and remotely controlled. The refrigerator takes approximately 140 min to cycle. Optimization of the fridge cycle has led to stable hold times well over 24 h at sea level with a full optical load. The operational hold time of the refrigerator was 36 h at the JCMT (4092 m) and 42 h at the higher elevation ASTE telescope (4860 m).

The refrigerator's ultra-cold (UC) stage, operating at a temperature of approximately 250 mK ($256.5 \pm 1.9 \pm 10$ mK where the 10 mK uncertainty comes from uncertainty in the calibration of the GRT), provides the thermal sink to the bolometer array. An intercooler (IC) stage, operating at approximately 360 mK, heat sinks an intermediate-temperature stage of the detector array support structure to thermally intercept heat flowing along the mechanical and electrical connections to the UC stage. Both the IC stage and the detector array assembly are thermally isolated and mechanically supported using two sets of short, hollow Vespel standoffs in a radial configuration. The resulting structure is extremely compact and stiff and the symmetry of the system prevents net motion of the optical axis under thermal contraction. The weakest vibrational mode of the support is along the optical axis and has a resonant frequency $>$400 Hz. The UC and IC temperatures showed no correlation with cryostat tilt or effective atmosphere optical depth during the JCMT observations.

The custom-designed AzTEC cryostat is a 'wet' system with liquid helium (23 litres) and liquid nitrogen (26 litres) tanks. The design and preparation of the cryostat resulted in operational (full loading, including daily fridge cycles) hold times of three days for liquid helium and over seven days for liquid nitrogen. The cryogen tanks are concentric annuli with near optimum length/diameter ratios to maximize their hold times. The inner diameter of the helium tank is 15.25 cm – a feature that adds valuable volume and accessibility to the shielded 4 K workspace without compromising cryogen capacity.

One challenge of working with semiconductor thermistors is the need to impedance transform using warm junction field-effect transisters (JFETs). AzTEC's low-noise U401 JFETs amplifier is suspended inside the inner diameter of the liquid helium tank by a set of reentrant G-10 tubes with tuned conductivity to allow the stage to self-heat to 130 K where the JFETs have empirically been found to exhibit low voltage and current noise. An intermediate stage of the suspension is sunk to the 77 K bath and intercepts the heat dissipated by the JFETs. These 130 and 77 K components are radiatively insulated with several layers of multilayer insulation (MLI). The inner wall of the 4 K helium tank is painted with an IR black paint to absorb stray thermal radiation.

The cryostat is designed to minimize electromagnetic/radio frequency interference (EMI/RFI) susceptibility. Two nested high-conductivity Faraday shields are formed through which all electrical connections pass via imbedded pi-filters. The 'cleanest' volume is bounded by the inner shield which surrounds the 4 K work volume. Custom compact in-line cryogenic pi-filters were constructed for AzTEC in coordination with the manufacturer. The outer Faraday cage is formed by the cryostat vacuum jacket and electronics enclosure.

2.2 Detectors

The AzTEC array is a 76 mm diameter monolithic silicon wafer containing 151 silicon nitride micromesh (spider-web) bolometers with neutron transmutation doped (NTD) Ge thermistors (Bock et al. 1996; Mauskopf et al. 1997; Turner et al. 2001). The wafer is organized into six pie-shaped regions (hextants) that together contain the 144 optically active bolometers and their wiring. The detectors are arranged in a close-packed hexagonal configuration with a spacing set by the detector feedhorn aperture of 5 mm. The bias for each detector is provided via a symmetric pair of 10 MΩ resistors contained in a separate module located close to the detector array. The seven 'blind' bolometers of the array are not biased or read out.

The bolometer behaviour is dictated by three sets of parameters: the thermistor properties, the amount of absorbed optical and electrical power and the thermal link between the bolometer and the cold heat sink of the cryostat. The thermal link is defined by an Au film deposited on one of the mesh support legs connected to the wafer substrate. Its heat conductance has the form $g_0 T^\beta$ with β in the range 1.2–1.6 (Glenn et al. 2003; Haig et al. 2004) where T is the bolometer operating temperature. The thermistor resistance has the form $R_0 \exp\sqrt{\Delta/T}$ with targeted R_0 and Δ values of 100 Ω and 42 K, respectively. In principle, g_0 as well as the electrical bias power are chosen to minimize detector noise given a known optical loading. For the AzTEC array, we chose a conservatively high g_0 that results in a heat conductance of 167 pW K^{-1} at 300 mK to mitigate the effects of any unanticipated excess optical loading and as a compromise for the different amounts of loading expected in the three possible optical passbands. For this choice, the noise equivalent power (NEP) predicted from our bolometer model for the optically loaded detectors is $5–7 \times 10^{-17}$ W/$\sqrt{\text{Hz}}$, which is comparable but subdominant to the photon-noise background limit (BLIP) in the 1.1 mm passband for anticipated operating conditions. The expected detector time constant, τ, of 3–4 ms also applies over the range of reasonable operating conditions. The thermistor resistance and bias resistor values are chosen such that the detector and

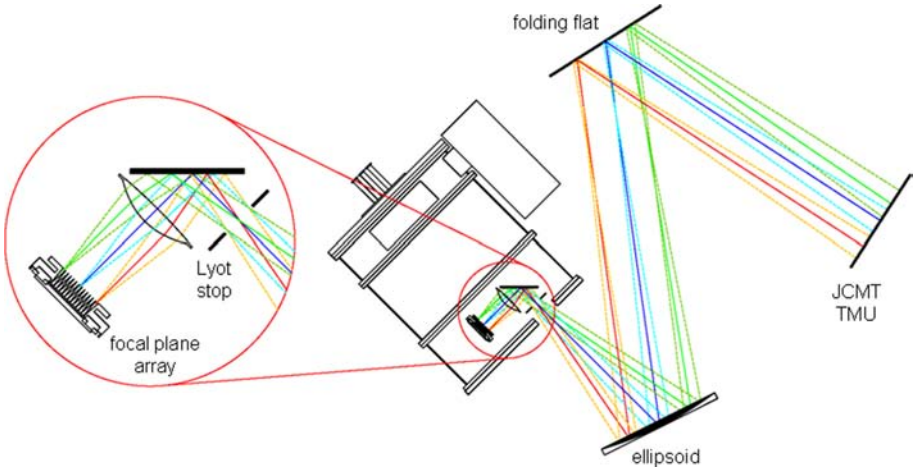

Figure 2. Schematic of AzTEC mounted in the JCMT receiver cabin with the associated coupling optics. All filters and mechanical supports have been omitted for clarity. Zemax-produced rays are shown for the central and outermost detectors in the plane of the drawing to illustrate the optical path of the various beams. The Cassegrain focus of the JCMT is located at the convergence of the beams just below the folding flat.

photon noise are dominant over noise sources from circuit elements further down the readout chain.

Once AzTEC is installed on a telescope, the only free parameter for optimising sensitivity is the amount of electrical (bias) power dissipated at the bolometer and hence the bolometer operating temperature T. Following Mather (1984), the balance between phonon noise, which rises with T, and Johnson noise, which falls steeply with rising T, results in an optimum value of the bias voltage for a given set of detector properties and a given optical loading. In practice, since there is a small spread in detector properties across the array and a slowly varying, but unpredictable, optical loading due to the atmosphere, we fixed the thermistor bias amplitude for all detectors in all hextants at 62.5 mV over the entire JCMT05B observing run. For an atmospheric optical depth at 225 GHz, τ_{225}, of 0.1, this conservatively high bias results in a sensitivity of 10 per cent worse than expected for a bolometer that has the design parameters. As shown in Section 5, nightly load curves, noise estimates and beam map observations during the JCMT05B run indicate that the detector sensitivity was near optimum over the entire observing run for this choice of bias.

2.3 Optics

A schematic diagram showing the relative positions of the optical elements with AzTEC in the JCMT receiver cabin is shown in Fig. 2. Our description of the coupling optics will start from the JCMT's tertiary mirror unit (TMU) located inside the receiver cabin. A complete list of JCMT optical specifications may be found on the JCMT web site. A list of optical constants for the AzTEC instrument and its JCMT coupling optics is given in Table 1.

At the JCMT, photons from the secondary mirror reflect off the TMU which is located behind the vertex of the primary mirror. For the AzTEC system, the TMU is oriented to direct the incoming beam upwards at an angle of 53.°2 with respect to the vertical. A flat-folding mirror then directs the beam downwards to an ellipsoidal mirror which converts the *f*/12 beam to an *f*/11.8 beam and directs the beam into the cryostat. The JCMT's Cassegrain focus resides between the folding flat and the ellipsoidal mirror. The AzTEC dewar is located such that a blackened Lyot stop, at a physical temperature of 4 K, is coincident with an image of the primary mirror. The image of the primary has a diameter of 52 mm and so the Lyot stop, which has a diameter of 50 mm, provides a cold guard ring to minimize the spillover at the primary mirror edge while allowing an aggressive edge taper. The folding flat and ellipsoidal coupling mirror are sized such that the edge taper of the outermost beam on each surface is less than −30 dB. Both mirrors and the cryostat are supported rigidly to minimize optical microphonic pickup.

Inside the cryostat, the detector array assembly is situated behind a 4 K biconvex aspheric lens fashioned from ultrahigh molecular weight polyethylene (UHMWPE) with index of refraction, $n = 1.52$. The lens surface is grooved with a series of concentric trenches of depth $\lambda/4\sqrt{n}$ which results in an antireflection surface tuned for the system passband. Considering the optical path in reverse, chief rays from each of the detectors' feedhorns are focused by the lens on to the centre of the blackened 4 K Lyot stop so that all detectors illuminate the 4 K edge of the Lyot stop with an edge taper of −5.2 dB in power. A 4 K folding mirror between the lens and the Lyot stop allows for a long optical path in a compact configuration to aid in keeping the overall structure mechanically rigid and isothermal.

The 250 mK bolometer array is mechanically and thermally supported between monolithic gold-plated aluminium arrays of tuned backshorts and feedhorns in a manner identical to that of the Bolocam instrument (Glenn et al. 2003). The array of backshorts and integrating cavities sets λ/4 behind the detectors in order to optimise detector absorption and minimize optical cross-talk between detectors (Glenn et al. 2002). The array of single-moded conical

Table 1. AzTEC design optical parameters for coupling to the JCMT. The calculation of the plane wave coupling efficiency at the Lyot stop is made assuming Gaussian optics and following the prescription of Goldsmith (1998).

Ellipsoid focal length	645.2 mm
Ellipsoid reflection angle	37°
UHMWPE lens focal length	163.6 mm
$f/\#_{\rm cass}$	12.0
$f/\#_{\rm Lyot}$	11.8
$f/\#_{\rm horns}$	3.2
Lyot stop diameter	50 mm
Edge taper at Lyot stop	−5.2 dB
Image of primary mirror dia.	52 mm
Plane wave coupling efficiency at Lyot stop	0.62
Detector spacing	$1.4f\lambda$

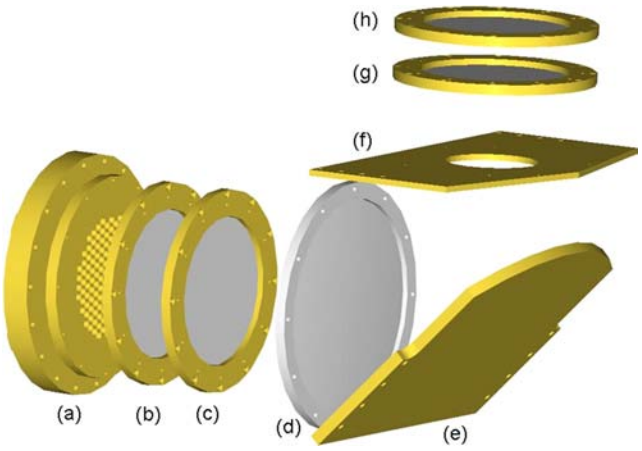

Figure 3. An exploded layout of the internal AzTEC optics. Components are: (a) integrated detector array, backshorts and conical feedhorns (250 mK); (b) 310 GHz low-pass filter (250 mK); (c) 360 GHz low-pass filter (250 mK); (d) bi-convex ultra-high molecular weight polyethylene lens (4 K); (e) folding flat (4 K); (f) 50 mm diameter Lyot stop (4 K) and (g and h) 390 and 1050 GHz low-pass filters (4 K). Not shown are an additional 77 K 540 GHz low-pass filter and a Zotefoam PPA-30 cryostat window.

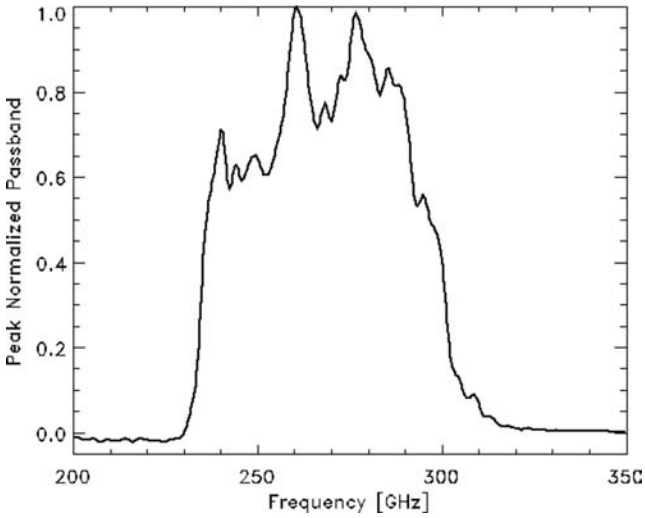

Figure 4. The AzTEC system bandpass for a flat spectrum input source, normalized to the peak response. (The low frequency portion of the spectrum is slightly negative due to a small phase offset in the Fourier transform spectrometer used to measure the response.)

feedhorns lies in front of the detectors and produces a set of quasi-Gaussian beams, each with Gaussian beam radius, w_a, of 1.84 mm at the horn aperture for the 1.1 mm wavelength configuration. This corresponds to an *f*/# for each horn of *f*/3.2.

2.3.1 Optical filtering

An exploded view of the internal optical layout including the filters is shown in Fig. 3. A short stub of single-mode waveguide (3.4 mm length for the 1.1 mm passband configuration) at the detector end of each horn provides the high-pass filter to the system passband. All of the low-pass filters in the system are quasi-optical metal mesh filters consisting of a series of resonant metallic meshes separated by transmission line sections. The resonant mesh filters are fabricated from thin copper films deposited on plastic (polypropylene or mylar) substrates and patterned into inductive or capacitive grids (Ade et al. 2006; Tucker & Ade 2006). In the 1.1 mm configuration, a set of low-pass filters, one rolling off at 360 GHz and the other rolling off at 310 GHz, is mounted to the feedhorn array and define the upper portion of the passband. For configurations with other band centres, the backshort array, the feedhorn array and these two low-pass filters are replaced.

Further optical filtering is required to suppress harmonic response from the 250 mK low-pass filters. A low-pass capacitive mesh filter (390 GHz edge) and an antireflection-coated 1050 GHz low-pass filter are mounted on the telescope side of the Lyot stop at 4 K. A 77 K, 540 GHz low-pass filter is mounted to the liquid nitrogen shield 2 cm further down the optical axis. Finally, a room temperature Zotefoam PPA30 (Zotefoams PLC) window provides IR scattering and a vacuum seal that is transparent at 1.1 mm wavelengths to better than 1 per cent according to in-lab measurements with a Fourier Transform Spectrometer. The resulting system passband is shown in Fig. 4. Measured optical characteristics are described further in Section 5.1.

2.4 Signal chain

A schematic for the detector signal chain is shown in Fig. 5. Each of the 144 bolometers is pseudo-current biased by a differential 200 Hz sine wave produced by a digital-to-analogue converter (DAC) – one DAC per hextant – and a pair of 10 MΩ load resistors. Noise in the bias is correlated across all detectors of a hextant and is removed in the data analysis. The bias frequency of 200 Hz is chosen to be fast compared to the detector time constant, $\tau > 3$ ms, but slow enough to avoid excessive attenuation from the effective low-pass RC filter arising from the bolometer/load resistor combination (∼3 MΩ) and the net parasitic capacitance of the signal lines and JFET gates ($C_{\rm parasitic} \sim 60$–110 pF).

Following each bolometer is a matched pair of low-noise U401 JFETs, in the source-follower configuration, that transforms the detector output impedance from several MΩ to ∼350 Ω. Signals from the JFET amplifiers exit the cryostat via pi-filters at 4 and 300 K and are read out by room-temperature, low-noise (1.7 nV $\rm Hz^{-1/2}$) instrumentation amplifiers (Texas Instruments, type INA103) with a fixed gain of 500. Each detector signal is then high-pass filtered at 100 Hz and low-pass filtered at 300 Hz before a programmable attenuation is applied by a digitally controlled resistive divider (see Fig. 5 for part numbers). The output of the divider is then digitized at 6.144 MHz by high-precision 24-bit delta-sigma A/D converters (Texas Instruments ADS1252) which produce an output data stream at a sampling rate of 16 kHz.

Once digitized, a Field Programmable Gate Array (FPGA) serializes each hextant's data into a single data stream. All processing up to this point happens in a custom electronics enclosure attached to the cryostat (the 'front-end' electronics). These data are sent via fibre optics to the off-cryostat back-end electronics where a single FPGA collects all six hextants' data streams. The back-end FPGA presents these data in parallel to a single Digital Signal Processor (DSP) for demodulation of each channel (twice) using the reference bias signal and its quadrature phase. The DSP caches the demodulated data streams in memory and applies a sharp block Finite Impulse Response filter, whose cut-off is just below the Nyquist frequency of the 64 Hz final sampling rate.

Bias generation and housekeeping electronics are also part of the front-end electronics located at the cryostat. The bolometer bias signal is generated from a digital sine wave stored in memory in the back-end FPGA and continuously fed via the fibre-optic connection to the DACs that generate the analogue sine wave for each hextant.

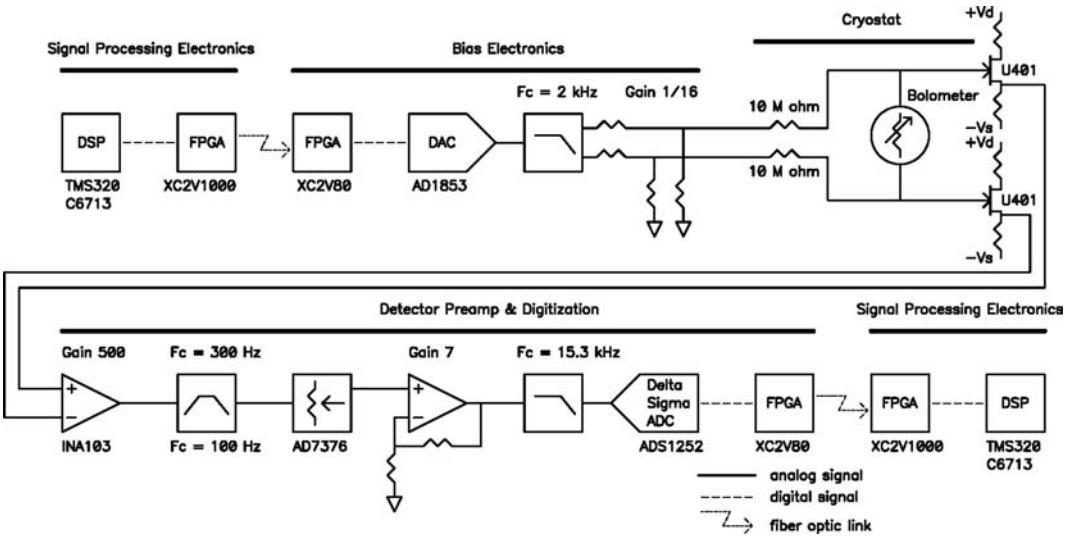

Figure 5. Schematic of the detector readout chain. All analogue electronics are replicated 144 times in the system.

The bias amplitude and phase are controlled digitally and in a real-time fashion. The bias frequency for the JCMT05B observations was 200 Hz. The housekeeping card reads out internal thermometer voltages, provides power and controls the ^{3}He refrigerator.

The back-end electronics are controlled by a dedicated Motorola Power-PC running the real-time VxWorks operating system. While a real-time system is not required by the data acquisition architecture, a real-time system simplifies synchronization of the native AzTEC signals with telescope pointing and other environmental signals. From the user's perspective, AzTEC is controlled and data are stored using a standard Linux PC running the Large Millimetre Telescope Monitor and Control (LMTMC) system which was developed at UMass-Amherst for general use by all LMT instruments (Souccar, Wallace & Malin 2004). All communication and data transfer between the Linux machine and the Power-PC is via dedicated Ethernet. Including pointing signals and telescope housekeeping signals, the total data rate of AzTEC is $\sim$80 kB s^{-1}.

3 OBSERVING

The AzTEC data set is logically grouped into 'observations' which include engineering tests (e.g. calibration, pointing, or focus observations) as well as scientific observations. All data are stored in a machine-independent binary format, Network Common Data Form (NetCDF). AzTEC NetCDF files are self-describing in that they include all information required to produce an optimal image, including header information defining the data as well as all observing parameters.

Real-time monitoring of AzTEC is conducted using various tools in the LMTMC package and the KST plotting suite. Quick-look software, custom written in the IDL programming language, is used to produce images immediately after the completion of each observation. These simple maps allow the user to quickly evaluate telescope pointing and focus, and provide an assessment of the overall quality of the data.

3.1 Observing modes

AzTEC is a passive instrument with respect to the telescope and operates completely independently of the observing mode. Since the mapping efficiency is a strong function of the observing mode and observing parameters for maps on-order the field of view of the instrument, we have adopted two primary modes in the existing data analysis suite.

3.1.1 Jiggle mapping

In the jiggle-mapping mode, the secondary mirror is chopped between on- and off-source sky positions while stepping through a series of small offsets (jiggles) to fill in gaps in coverage left by the approximately 20 arcsec spacing of the detectors. Differencing chopped data at a single jiggle position remove the effects of low-frequency atmospheric and instrumental drifts. Chop frequencies during the JCMT05B run ranged from 2 to 4 Hz with a secondary mirror transit time of less than 30 ms, and a jiggle frequency of 1 Hz. Once the full jiggle pattern is completed, the primary mirror 'nods' to put the off-source beams on source. Averaging data from opposite nods further suppress differential pickup from spillover at the primary mirror, temperature gradients on the primary and scattering from the secondary support structure.

For fields on the same scale as the array field of view (FOV) or smaller, jiggle mapping is the highest efficiency observing mode for a given target sensitivity. However, when imaging fields that are much larger than the array FOV, the overheads of jiggle mapping and the high variability in coverage make scan mapping essential. The coverage map from a jiggle map is highly sensitive to the distribution of detector sensitivities on the array. This is particularly evident in AzTEC jiggle maps taken during the JCMT05B observing run, as shown in Figs 6 and 7, where a contiguous region of detectors was inoperable. This resulted in a portion of the field being severely undersampled. For jiggle-map observations of sources with a known location, we adjust for the non-uniform coverage by offsetting the boresight pointing of the telescope so that the target falls in a region fully populated by working detectors.

3.1.2 Raster scanning

For raster-scan observation, the telescope boresight sweeps across the sky along one direction, takes a small step in the orthogonal direction and then sweeps back along the next row of the scan. This

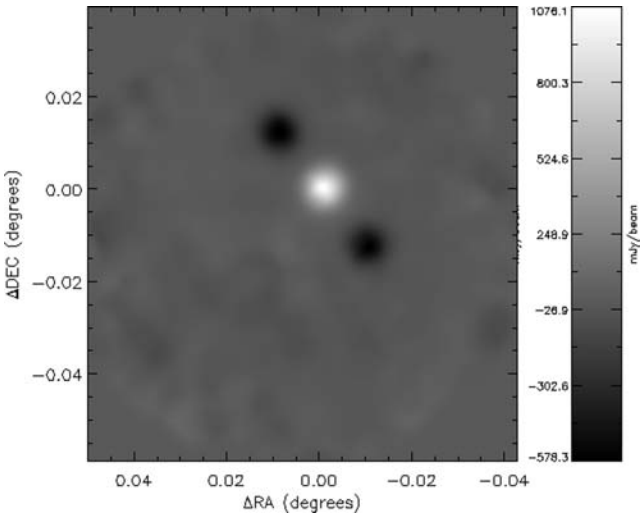

Figure 6. Jiggle map of QSO J1048+7143. A Gaussian fitted to the peak flux gives the telescope boresight offset from the reference bolometer (Section 3.2.4).

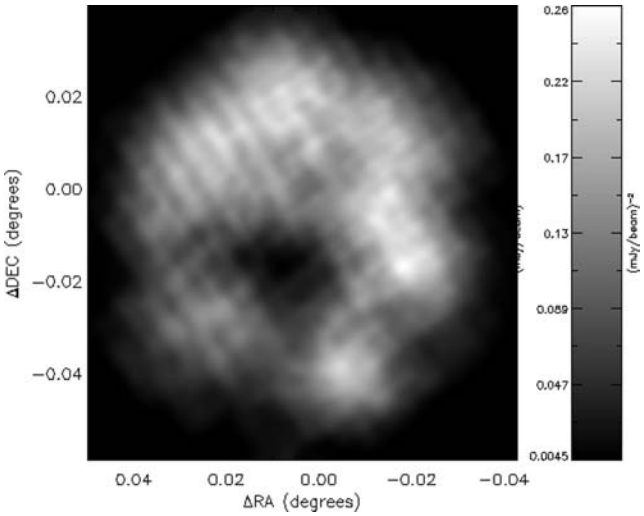

Figure 7. The corresponding weight map (in mJy beam^{-2}) for the signal map in Fig. 6. The lack of coverage due to a clustering of inactive detectors is indicated by the low weight region near the centre of the map.

pattern is repeated until the entire field has been imaged. Because of the low-frequency stability of the detectors, we do not chop the secondary mirror. In fields where no bright sources are expected, the removal of the atmospheric contamination is currently accomplished via a principal component analysis (PCA) of the full data stream on a scan-by-scan basis (Laurent et al. 2005). The PCA technique is used in the analyses leading to the instrument performance and characteristics detailed in Section 5.

The major benefit of raster scanning is in the ability to map a large area of sky in a single observation with a very uniform coverage, as shown in Fig. 8. The distribution of inoperable detectors on the array only affects the ultimate sensitivity of the map, and not the uniformity of the coverage in the map. Scan speeds are limited by the detector time constant and stability of the telescope but are generally chosen based on the science target and the atmospheric opacity. For point source observations at the JCMT05B run, high scan speeds were preferred in order to move the signal bandwidth

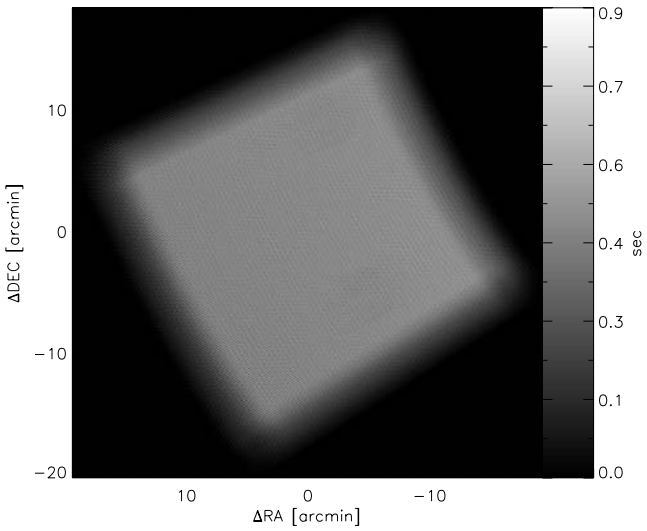

Figure 8. The integration time in each 2 arcsec pixel for a 25 × 25 arcmin^2 raster-scan map with scanning done in the elevation direction and with 10 arcsec step sizes in azimuth, demonstrating the uniform coverage achieved with this observing mode.

above the knee frequency of residual atmospheric contamination (see Fig. 14), however at a cost in overall observing efficiency due to the fixed length turnaround time (5 s) of the telescope. Co-adding tens of raster-scanned maps taken with different sky position angles reduces scan-synchronous effects in the maps and offers excellent cross-linking of the data.

3.2 Observing overheads

While AzTEC was on the JCMT, the following ancillary observations were made, averaging 24.7 per cent of the total available observing time.

3.2.1 Focus observations

Focus measurements consist of a series of jiggle-map observations on a bright (∼a few Jy) point source as the secondary mirror steps through different focus settings. For each focus setting, we fit a two-dimensional Gaussian to the region of the image containing the source. The optimal focus location is the secondary position where the beam full-width at half maximum (FWHM) is minimized and the peak amplitude of the signal is maximized. For the JCMT05B run, we focused the telescope at the beginning and mid-way through each night of observing.

3.2.2 Relative bolometer offsets

Since the array orientation is fixed in azimuth and elevation, the relative offset on the sky between any two detectors is constant. We determine these offsets by mapping a bright point source each evening prior to science observations and after focusing the telescope. A high-resolution map is made such that the point spread function (PSF) of each detector in the array is sampled with at least 4 arcsec resolution in order to determine the relative bolometer positions to an accuracy of ≈5 per cent of the PSF FWHM. These 'beam map' observations also provide the absolute calibration of detectors in the array (see Section 4).

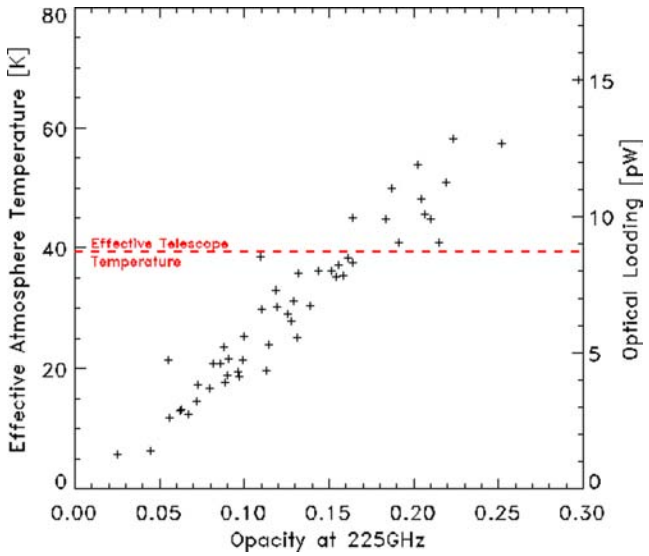

Figure 9. The effective atmosphere temperature in the 1.1 mm AzTEC bandpass as a function of the atmospheric opacity at 225 GHz as measured by the CSO. The axis on the right-hand side gives the corresponding amount of optical power absorbed by the AzTEC detectors. The horizontal line shows the effective temperature/power of the telescope and coupling optics.

3.2.3 Load curves

Load curve measurements – sweeping the detector bias through its full range of commandable values while viewing a blank patch of sky – are made each evening following the determination of the relative bolometer offsets. From the load curves, we determine the total optical power, Q, absorbed by each detector as well as the responsivity, S (the conversion from Volts read out of the detector to Watts absorbed) of each detector. By measuring the responsivity in this manner under a wide range of atmospheric opacities, we construct a correction to the non-linearity of the detector response due to the overall variation in the atmospheric optical loading. This process is described further in Section 4.1.

Fig. 9 shows the contributions of the atmosphere and other sources to the total optical power absorbed by the AzTEC detectors. The telescope, coupling optics and any parasitic optical loadings on the detectors deliver a combined 9 pW of power – corresponding to an effective blackbody temperature of 39 K. The optical loading due to the atmosphere is linear with the opacity as measured by the Caltech Submillimetre Observatory (CSO) tau metre at 225 GHz over the range of opacities suitable for observing.

3.2.4 Pointing observations

Pointing measurements are performed approximately every hour in order to measure the absolute pointing offset between the telescope boresight and a reference bolometer. An optimal pointing source is bright ($\geqslant$1 Jy), unresolved and located near the science target. Pointing observations typically bracketed a series of science observations so that slow drifts in the residuals to the telescope pointing model could be fit out. Since only a few bolometers must pass over the source, pointing observations are usually carried out in jiggle-map mode. We fit a two-dimensional Gaussian to the point source image, and the best-fitting location of the peak signal gives the boresight offset as shown in Fig. 6. To correct the pointing signals for a given science observation, a pointing model is generated by interpolating between the pointing measurements taken over a night.

4 CALIBRATION

The output of bolometer i at sky position α, $b_{i,\alpha}$ (in units of V), is given by

$$b_{i,\alpha} = S_i(Q) A_{\rm eff} \eta \int_0^\infty {\rm d}\nu\, f(\nu) \int_{\rm sky} {\rm d}\Omega P_i(\Omega_\alpha - \Omega) e^{-\tau_{\rm eff}} I_\nu(\Omega), \quad (1)$$

where $S_i(Q)$ is the responsivity (in V/W), Q is the optical loading (in W) dominated by the telescope and atmosphere, $A_{\rm eff}$ is the effective telescope aperture, η is the optical efficiency, $f(\nu)$ is the peak-normalized AzTEC bandpass, $P_i(\Omega_\alpha - \Omega)$ is the peak-normalized AzTEC beam pattern for bolometer i at sky position Ω_α, $\tau_{\rm eff}$ is the opacity and $I_\nu(\Omega)$ is the source intensity on the sky (in Jy beam^{-1}). As discussed below, S_i and $\tau_{\rm eff}$, both of which depend on observational conditions (e.g. weather) and change significantly on the time-scale of hours, are modelled as functions of the 'dc' level of the bolometer signal.

The flux conversion factor for bolometer i, FCF$_i$ (in units of Jy beam^{-1} W^{-1}), is an expression involving all factors that are, in principle, constant (i.e. source and weather independent) over the entire observing run, and is defined as

$${\rm FCF}_i = \frac{1}{A_{\rm eff}\eta \int_0^\infty {\rm d}\nu\, f(\nu) \int_{\rm sky} {\rm d}\Omega\, P_i(\Omega_\alpha - \Omega)}. \quad (2)$$

For a point source located at (θ_0, ϕ_0) with average flux density $\bar{I}$ over the optical bandpass, the bolometer output is

$$b_i(\theta_0, \phi_0) = \frac{S_i(Q) e^{-\tau_{\rm eff}} \bar{I}}{{\rm FCF}_i}. \quad (3)$$

4.1 Responsivity and extinction corrections

The optical loading on the detectors and the bolometer responsivities are determined from load curve measurements (see Section 3.2.3). For the range of total power loading on the detectors observed during the JCMT05B run, the responsivity is linearly proportional to the demodulated dc-level of each bolometer's time-stream signal. The responsivity of a typical bolometer versus the dc-level measured from all of the load curve observations taken during the JCMT05B run is shown in the left-hand panel of Fig. 10. The solid curve shows the linear fit to the measurements. We derive the best-fitting offset and slope for each bolometer separately since the spread in these parameters is large compared to the formal errors on the fits.

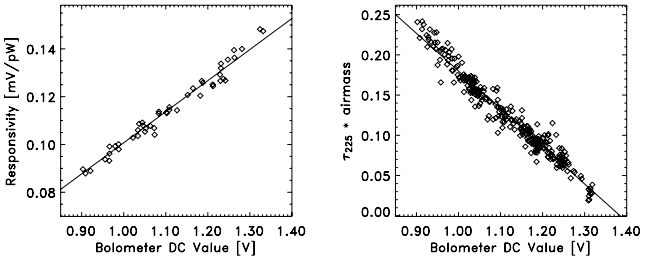

Figure 10. Left-hand panel: responsivity versus bolometer dc-level for a typical detector as determined from all of the load curves taken during the JCMT05B run. A best-fitting line is overplotted. Right-hand panel: opacity versus bolometer dc-level for the same detector.

The atmospheric extinction $e^{-\tau_{\rm eff}}$ is corrected in a similar way. A linear correlation exists between the atmospheric opacity, $\tau_{\rm eff}$ and the bolometer dc-signals (see right-hand panel of Fig. 10). For the JCMT data, we use the atmospheric opacity at 225 GHz as determined from the CSO tau monitor, which records $\tau_{225\rm GHz}$ (zenith) every 10 min, to calibrate the relation with the bolometer dc-levels.

4.2 Measured FCF from beam map observations

To determine the flux conversion factor for each bolometer, $\rm FCF_{\it i}$, we beam map a primary or secondary flux calibrator each night. The time-stream bolometer signals are corrected for extinction and the responsivity is factored out. An iterative cleaning technique is used to minimize errors in fitted parameters due to atmospheric contamination. In the final iteration, maps are made for each bolometer separately and we fit a two-dimensional Gaussian to each map. The best-fitting amplitude combined with the known flux of the source gives the FCF for each detector.

To correct the flux for the angular size of Uranus, we assume that Uranus is a disc with angular radius $\Theta_{\rm U}$ and brightness temperature $T_{\rm b}$ so that $I(\Omega) = T_{\rm b}\Phi(\Omega)$, where $\Phi(\Omega) = 1$ for $\theta \leqslant \Theta_{\rm U}$ and 0 otherwise and $T_{\rm b} = 92.6 \pm 1.7$ K (Griffin & Orton 1993). The average flux of Uranus for bolometer i is then given by

$$\bar{I} = \frac{\int_0^\infty {\rm d}\nu\ f(\nu)\frac{2kT_{{\rm b},o}\nu^2}{c^2}\int_{\rm sky}{\rm d}\Omega\ P_i(\Omega_\alpha - \Omega)\Phi(\Omega)}{\int_0^\infty {\rm d}\nu\ f(\nu)\int_{\rm sky}{\rm d}\Omega\ P_i(\Omega_\alpha - \Omega)}, \quad (4)$$

which can then be used in equation (3). Uranus is small compared to the AzTEC detector PSFs on the JCMT ($2\Theta_{\rm U} \ll \theta_{{\rm b}_i}$, where $\theta_{{\rm b}_i}$ is the true beam FWHM for bolometer i) and so will appear approximately Gaussian with a measured FWHM θ_{m_i}, where

$$\theta_{{\rm b}_i}^2 = \theta_{m_i}^2 - \frac{\ln 2}{2}(2\Theta_{\rm U})^2 \quad (5)$$

(Baars 1973). We measure θ_{m_i} from Uranus beam maps, and use equation (5) to determine $\theta_{{\rm b}_i}$ and subsequently $\rm P_{\it i}(\Omega)$. We then calculate the integral in equation (4) to determine the correction factor for the flux of Uranus.

For beam maps of Uranus, there is a statistically significant increase in the measured $\rm FCF_{\it i}$ for measurements taken within one hour after sunset at the JCMT. Measurements taken after this time have constant $\rm FCF_{\it i}$. This is consistent with rough estimates of the telescope's thermal time constant. For this reason, we determine the average flux conversion factor for each bolometer $\langle \rm FCF_{\it i}\rangle$ by averaging over all $\rm FCF_{\it i}$ measured from Uranus beam maps taken $\geqslant$1 h after sunset, and we use these values to calibrate all science observations taken after the telescope has settled. A linear correction factor derived from beam maps taken within one hour after sunset is applied to science data taken during this period. We model this correction factor $f \equiv \rm FCF_{\it i}/\langle FCF_{\it i}\rangle$ as a linear function of the time after sunset, such that

$$\begin{aligned} f &= 1 && \text{if HAS} \geqslant 1 \\ &= 1 + m(\text{HAS} - 1) && \text{if HAS} < 1 \end{aligned} \quad (6)$$

where HAS is the time after sunset measured in hours, m is the same for all bolometers, and continuity at HAS = 1 has been applied. We fit the measured $\rm FCF_{\it i}/\langle FCF_{\it i}\rangle$ for all bolometers and all beam maps with HAS < 1 simultaneously to equation (6) to find $m = -0.115 \pm 0.002\,h^{-1}$.

4.3 Calibration error

For a given science observation with responsivity S_i and extinction $e^{-\tau_{\rm eff}}$ (measured from the bolometer dc-levels), the calibrated time-stream bolometer signals $\bar{I}_i(t)$ are given by

$$\bar{I}_i(t) = \frac{b_i(t)\langle \rm FCF_{\it i}\rangle f}{S_i e^{-\tau_{\rm eff}}} \quad (7)$$

where f is determined from the HAS that the observation took place and the empirical formula derived above (equation 6). The error on the calibrated bolometer signals is therefore equal to the quadrature sum of the errors on all four factors in equation (7) and is typically 6–13 per cent for the JCMT05B data.

5 PERFORMANCE

5.1 Array layout and system efficiency

The array 'footprint' on the sky for the JCMT05B run is shown in Fig. 11, centred on the reference bolometer and with the six hextants labelled. We exclude all detectors that were not fully operational during this run, most of which are located in Hextants 1 and 2. This left us with 107 operational pixels for the JCMT05B season. The majority of failures in the signal chains have recently been traced to broken JFETs and these are expected to be repaired by 2009.

Each bolometer's location on the array and its PSF are determined from beam map observations as described in Section 3.2.2. The positions and beam sizes displayed in Fig. 11 were determined by averaging the measurements from all beam maps of Uranus taken at the JCMT. The size of the ellipse is equal to the beam FWHM, which is measured in the azimuth and elevation directions and is on average 17 ± 1 arcsec in azimuth and 18 ± 1 arcsec in elevation at the JCMT. An off-axis ellipsoidal mirror in the optics chain leads to the slight elongation of the beam in the elevation direction. The array FOV is roughly circular with a diameter of 5 arcmin. A constant azimuth cut through a typical bolometer's beam map is shown in

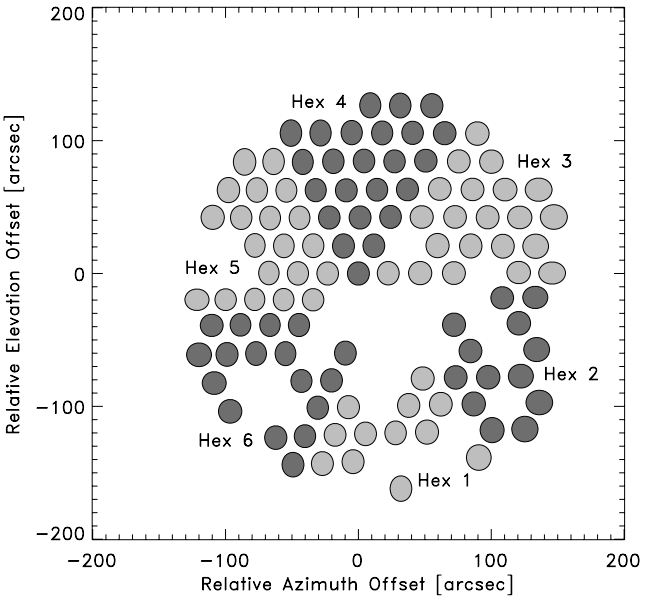

Figure 11. AzTEC's 'footprint' on the sky at the JCMT05B run. The six hextants are labelled 'Hex' 1–6. The alternate shading indicates which bolometers are located in each hextant. The size of the ellipse corresponds to the bolometer's FWHM, measured in the azimuth and elevation directions.

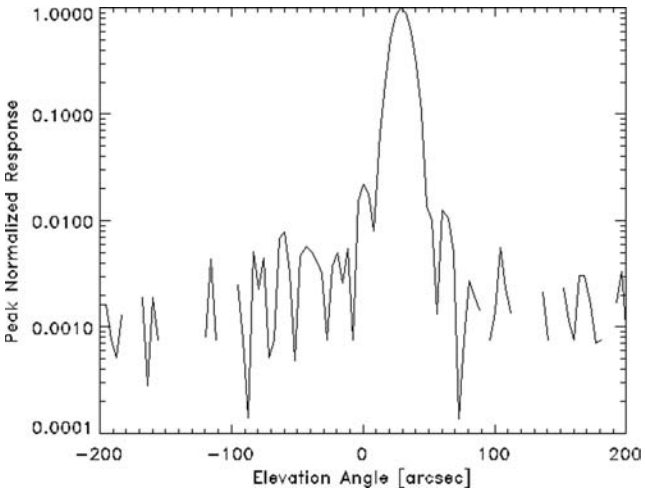

Figure 12. A cut in the elevation direction through the beam response pattern of a typical AzTEC pixel.

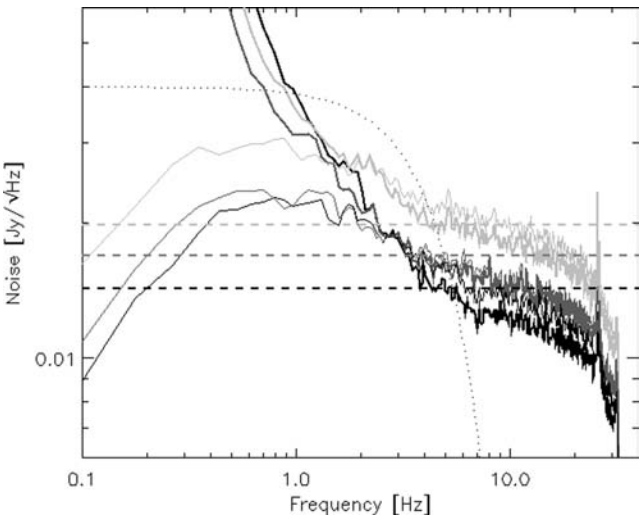

Figure 13. The NEFD for a typical bolometer. In order of decreasing darkness, the three shades correspond to effective τ_{225} values of 0.11, 0.16 and 0.21. The thicker curves represent raw data while the thinner curves show data that have been cleaned using a PCA. The cleaned noise spectra are higher at some frequencies because they have been scaled to account for point-source attenuation due to cleaning. The lower-opacity data benefit more from the common-mode removal effected by cleaning as well as by the reduced optical loading. The dashed lines represent the corresponding NEFDs for a detector with targeted detector parameter values at our JCMT bias level along with an estimate of optical loading (details in the text). The dotted curve indicates the approximate optical bandwidth of a point source (in arbitrary units) for a scan velocity of 180 arcsec s^{-1}.

Table 2. AzTEC 1.1 mm optical parameters for the JCMT05B observations. The effective bandwidth is calculated assuming a flat-spectrum source.

Band centre frequency	270.5 GHz
Effective bandwidth	49.0 GHz
Effective throughput ($A\Omega\eta$)	0.2 ± 0.014 mm^2 sr
Beam FWHM (azimuth)	17 ± 1 arcsec
Beam FWHM (elevation)	18 ± 1 arcsec

Fig. 12. The beams are nicely Gaussian down to the first sidelobe response at ~ -20 dB.

Table 2 lists the measured optical characteristics of AzTEC in the 1.1 mm configuration for the JCMT05B observations. The effective throughput ($A\Omega\eta$) is measured for each detector from each beam map of Uranus. It is calculated using equation (2) along with AzTEC's measured bandpass, $f(\nu)$ and the measured flux conversion factor of that detector, FCF_i. The value listed in Table 2 is an average over all working detectors.

The optical efficiency η of the system may be written as the product of the telescope's efficiency, η_{tel}, and the coupling efficiency of the instrument η_{inst}. We estimate the telescope emissivity, ϵ, as the ratio between the effective telescope temperature of Fig. 9 (dashed line) and the true average temperature of the telescope surface. This emissivity estimate gives $\eta_{\mathrm{tel}} = 1 - \epsilon = 0.85$. Removing this factor from the total throughput, we find that the *instrument throughput*, $A\Omega\eta_{\mathrm{inst}}$, is 0.23 mm^2 sr. Comparing this to the idealized throughput of a single-moded system at 1.1 mm wavelength with the same telescope efficiency ($A\Omega\eta_{\mathrm{tel}} = \lambda^2\eta_{\mathrm{tel}} = 0.99$), we find the optical efficiency for the AzTEC radiometer to be 0.19. Given that the cold Lyot stop leads to a 38 per cent reduction in throughput, this leaves an overall efficiency of 31 per cent. This is very similar to the optical efficiency measured for the Bolocam instrument (Glenn et al. 2003) which has a very similar optical design.

5.2 Noise and sensitivity

Blank field observations done in raster-scan mode are used to estimate detector noise and sensitivity. Fig. 13 shows the noise equivalent flux density per beam (NEFD) for a typical detector in three weather conditions at the JCMT. The thicker curves show the raw NEFDs while the thinner curves of the same shade show the improvement due to a time-stream cleaning method based on a PCA. The low-frequency features, dominated by atmospheric fluctuations, are not completely projected out by the PCA cleaning. The flatter NEFD at higher frequencies that does not benefit from cleaning can be attributed to the irreducible noise floor due to the photon background limit (BLIP) and detector noise.

The three dashed lines indicate the thermodynamic noise limits for an ideal AzTEC detector given the bias voltage, expected atmospheric optical loading for three opacities and optical loading from the telescope (assuming a 15 per cent effective emissivity). In each case, the actual high-frequency noise level is consistent with the detector and loading model to within 10–20 per cent, well within our uncertainty of the total optical loading on the detectors. The nearly constant ratio between the achieved and expected noise levels over varying weather conditions indicates that the operationally convenient choice of using a constant bias voltage for the entire observing run (see Section 2.2) had little if any negative impact on sensitivity. Table 3 lists the expected detector operating parameters and the breakdown of thermodynamic noise contributions for conditions at the JCMT assuming $\tau_{225} = 0.11$. The actual post-cleaning NEP measured for a typical detector is dominated by residual low-frequency noise due to the atmosphere and, based on our point-source sensitivity, is equivalent to having a white noise level of 1846 aW/$\sqrt{\mathrm{Hz}}$.

The increase in noise at low frequency highlights the importance of scanning at high speed. The dotted curve of Fig. 13 indicates the approximate optical bandpass of a detector at a scan velocity of 180 arcsec s^{-1}, which is also the detector response to a point source at that scan speed. Throughout the course of the observing run, we

Table 3. The nominal operational values for detector temperature (T), thermistor resistance (R), thermal-link conductance (g) and bolometer responsivity (S) are given at the top. They are calculated according to the detector parameters and operating bias given in Section 2.2 and the atmospheric loading expected from a τ_{225} (opacity) of 0.11 given the optical characteristics of Table 2. Also tabulated is the expected breakdown of thermodynamic noise contributions. They are calculated by using the above operating parameters according to the equations of Mather (1984). Because noise is quoted in terms of NEP *absorbed at the detector*, the optical parameters of Table 2 must be used for converting these to noise-equivalent surface brightness or flux density (as in Table 4).

T (mK)	R (MΩ)	g (pW K^{-1})	S (V W^{-1})
438	1.79	295	1.22×10^8

Johnson noise	34 aW/$\sqrt{\text{Hz}}$
Phonon noise	44 aW/$\sqrt{\text{Hz}}$
Amplifier	58 aW/$\sqrt{\text{Hz}}$
Load resistor	4 aW/$\sqrt{\text{Hz}}$
Photon noise	102 aW/$\sqrt{\text{Hz}}$
Total:	130 aW/$\sqrt{\text{Hz}}$

used scan speeds from 30 to 270 arcsec s^{-1} based on balancing the opposing effects of higher sensitivity and larger turnaround time fraction at higher scan speeds given a map size, as explained in Section 3.1.2. With scans along the elevation direction, we do not see vibration-induced noise increase within this range of velocities during the JCMT05B observations. We did measure excess noise near ∼2 Hz on bad-weather nights at the JCMT, possibly due to wind-induced small motions of optical loads and/or optics, like the JCMT's Gore-tex cover.

The abrupt noise cut-off near 32 Hz is due to a digital filter that conditions the demodulated bolometer signals for 64-Hz decimation. The attenuation with frequency between 20 and 30 Hz is due to the bolometer time constant. The line at ∼25 Hz is likely a side band caused by the third harmonic of AC power (or '60 Hz') mixed with the 200 Hz demodulation waveform. When analysing raster-scan observations, we implement a second digital low-pass filter in software to avoid aliasing this power back into the signal bandwidth.

The 'flat' NEFDs near 10 Hz represent a limiting white noise level regardless of how effectively the low-frequency atmospheric features can be removed using a particular cleaning method. Therefore, in Fig. 14 we have histogrammed these ultimate sensitivities for the working detectors. The particular detector whose NEFD is shown in Fig. 13 falls within one of the better populated (tallest) bins of Fig. 14 in all three weather conditions.

5.3 Mapping speed and instrument sensitivity

The best indicator of future performance and capability for an array receiver is the instrument mapping speed. Mapping speed is a metric that can be summed linearly and simultaneously accounts for the variations in detector sensitivities, the effectiveness of the atmospheric cleaning algorithm, the individual optical efficiencies achieved by each detector and, most importantly, the residual correlations between detectors in the array. We calculate the effective mapping speed for our JCMT raster-scanned maps as

$$M_{\rm em} = \frac{N_{\rm det}\Omega_{\rm pix}}{t_{\rm int}} \sum_{i=1}^{N_{\rm pix}} \frac{1}{\sigma_i^2}, \quad (8)$$

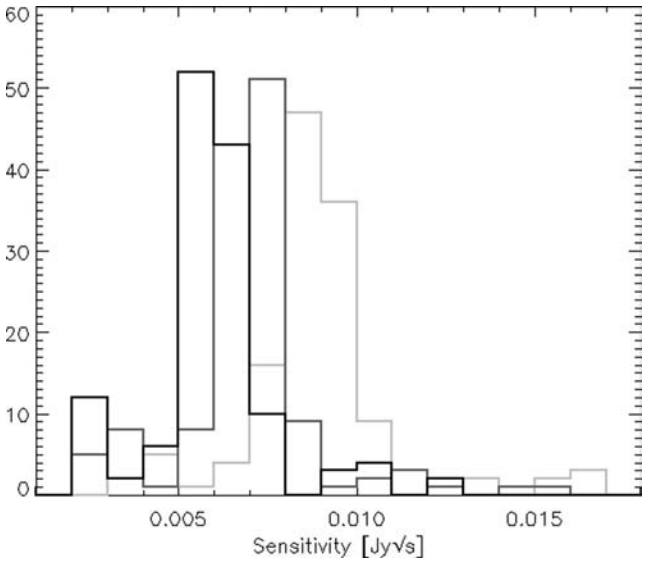

Figure 14. Histogram of the ultimate sensitivity of working detectors for three different effective opacities using the higher frequency 'flat' noise level of raw data as seen in Fig. 13.

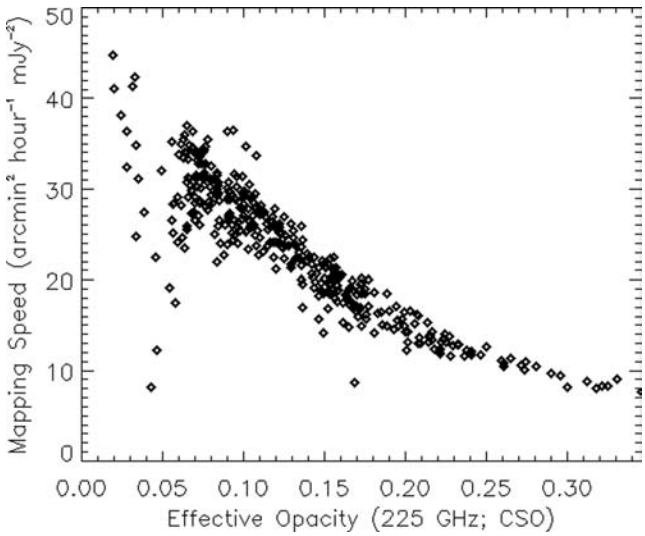

Figure 15. Empirical point-source mapping speeds for the AzTEC/JCMT system for a variety of atmospheric opacities and using the current cleaning/mapping software. These mapping speeds were calculated according to equation (8) and do not include overheads and mapping efficiencies that are specific to the observing strategy employed. Here, σ_i is taken as the raw (unfiltered) pixel noise scaled by the expected gain due to an optimal point-source filter after co-addition (see text for details).

where σ_i represents the noise level of the ith pixel in a map with $N_{\rm pix}$ pixels of solid angle $\Omega_{\rm pix}$, $N_{\rm det}$ represents the number of functional detectors and $t_{\rm int}$ is the total integration time spent on a field.

Point-source mapping speeds achieved through raster scanning of the JCMT05B observations of large blank fields are plotted in Fig. 15. Most overheads and mapping efficiencies are ignored, making these idealized speeds generally applicable to raster-scanned AzTEC maps at any observatory by scaling the mapping speed values by the ratio of the telescope areas (assuming similar telescope efficiencies).

Table 4. Expected and achieved noise performance. 'Projected' is the (white) time-stream PSD prediction based on the bolometer model and optical loading. Values in parentheses are calculated for the LMT by scaling according to telescope area assuming an effective LMT mirror diameter of 43 m as (very conservatively) truncated by AzTEC's Lyot stop. 'Measured (white PSD level)' is the noise level measured from calibrated time-stream PSDs at 10 Hz from the $\tau_{225} = 0.11$ *thicker* curve of Fig. 13. 'Measured (actual PSD)' is the inferred sensitivity based on the full cleaned time-stream PSD of the $\tau_{225} = 0.11$ *thinner* curve of Fig. 13. The quoted sensitivity is calculated by forming a weighted average of PSD/2, weighted by the square of the point-source response function of Fig. 13, and then taking the square root. 'Measured (map space)' is the sensitivity inferred from mapping speeds estimated with equation (8). Values given in bold are directly computed from AzTEC data. All other values are estimated as described in the text.

	Projected (bolometer model) JCMT (LMT)	Measured (white PSD level) JCMT	Measured (actual PSD) JCMT	Measured (map space) JCMT	
Detector sensitivity	10.02 (0.9)	8.55	**14.5**	26–28	mJy$\sqrt{\text{s}}$
Mapping speed	184 (2013)	253	88	**23–28**	arcmin^2 mJy^{-2} h^{-1}

It is generally favourable to apply a point-source filter *after* the co-addition of multiple raster-scanned maps due to the benefits of cross-linking. To estimate effective mapping speeds of the individual observations presented in Fig. 15, σ_i values of the resulting map are estimated as the unfiltered pixel noise scaled by the average reduction factor due to our optimum filter when applied to a co-added map.

Mapping speed is correlated to the atmospheric conditions in two ways: atmospheric loading (shot noise) and atmospheric stability. The latter gives rise to residual fluctuations that are inseparable from astronomical signals which leads to much of the scatter in the mapping speeds. The high scatter in mapping speeds at the lowest opacities is in part due to errors in the estimation of the opacity. There is no significant evidence that the trend of mapping speed with opacity breaks down for the lowest opacities.

Table 4 gives the expected and achieved noise performance of the instrument in a manner that allows one to compare ideal and achieved detector sensitivities and mapping speeds in terms of flux density. In the table, the column of 'projected' sensitivities indicates the sensitivity predicted from the bolometer model and the measured optical loading at the JCMT. The three columns of measured sensitivities show the achieved sensitivities in the presence of atmospheric noise in three cases: (i) if 'perfect' atmospheric noise subtraction were possible as measured by the 10-Hz value of the time-stream detector noise of Fig. 13, (ii) with the achieved atmospheric noise subtraction indicated by the thinner power spectral density (PSD) curves of Fig. 13 and the point-source response function (also shown as a dotted curve in that figure) and (iii) as inferred from empirical mapping speed estimates obtained with equation (8). We use the following relationship between mapping speed and detector sensitivity $\hat{s}$ (in mJy$\sqrt{s}$) to calculate one where the other is known:

$$\text{MS} = \frac{3600 N_{\text{det}} \Omega_{\text{b}}}{2\hat{s}^2}, \tag{9}$$

where $N_{\text{det}} = 107$ and $\Omega_{\text{b}} = 0.096$ arcmin^2, the area under an 18 arcsec FWHM two-dimensional Gaussian. Equation (9) assumes the use of a simple beam-smoothing filter on maps. The factor of $2\hat{s}^2$ in the denominator represents the square of $\hat{s}_{\text{sm}}(=\sqrt{2}\hat{s})$, the appropriate sensitivity post smoothing.

The degradation of sensitivity and mapping speed between Columns 3 and 4 is believed to be due to non-idealities such as residual bolometer–bolometer correlations which are not apparent from the time-stream PSDs. We emphasize that Column 4 of Table 4, or more generally, Fig. 15, properly scaled by telescope area, is the most accurate reference for planning observations with AzTEC. The values given in Table 4 are only meant to be illustrative of where the losses in sensitivity occur when beginning projections with raw detector sensitivities.

6 FUTURE

AzTEC completed a successful three-month scientific run on JCMT from 2005 November to 2006 February. Reduction and analysis of the various data sets acquired during the run are being completed. AzTEC is now a facility instrument at the 10 m ASTE (a Japanese ALMA prototype telescope) for observations during the South American winters of 2007 and 2008. AzTEC will be delivered to the 50 m LMT in early 2009, where it will serve as a first-light instrument at 2 and 1 mm wavelengths, and then become a facility instrument for general use in all three of its wavebands.

ACKNOWLEDGMENTS

We acknowledge the following people for their various and valuable contributions to the success of the AzTEC instrument and/or AzTEC observations: Itziar Aretxaga, Cara Battersby, Yuxi Chen, Iain Coulson, Gary Davis, Simon Doyle, Daniel Ferrusca, Douglas Haig, Salman Hameed, David Hughes, John Karakla, James Lowenthal, Gary Wallace and Miguel Valazquez. SK and YK were supported in part by Korea Science & Engineering Foundation (KOSEF) under a cooperative agreement with the Astrophysical Research Centre of the Structure and Evolution of the Cosmos (ARCSEC). This work was supported in part by NSF Grant 0540852.

REFERENCES

Ade P. A. R., Pisano G., Tucker C., Weaver S., 2006, in Zmuidzinas J., Holland W. S., Withington S., Duncan W. D., eds, Proc. SPIE Vol. 6275, Millimeter and Submillimeter Detectors and Instrumentation for Astronomy III. SPIE, Bellingham, p. 62750U

Baars J. W. M., 1973, IEEE Trans. Antennas Propag., AP-21, 461

Bhatia R. S. et al., 2000, Cryogenics, 40, 685

Bock J. J., Delcastillo H. M., Turner A. D., Beeman J. W., Lange A. E., Mauskopf P. D., 1996, in Rolfe E. J., Pilbratt G., eds, ESA SP-388, Submillimetre and Far-Infrared Space Instrumentation. ESA, Paris, p. 119

Glenn J., Chattopadhyay G., Edgington S. F., Lange A. E., Bock J. J., Mauskopf P. D., Lee A. T., 2002, Appl. Opt., 41, 136

Glenn J. et al., 2003, in Phillips T. G., Zmuidzinas J., eds, Proc. SPIE Vol. 4855, Millimeter and Submillimeter Detectors for Astronomy. SPIE, Bellingham, p. 30

Goldsmith P., 1998, Quasioptical Systems. IEEE, NY

Griffin M. J., Orton G. S., 1993, Icarus, 105, 537

Haig D. J. et al., 2004, in Bradford C. M. et al., eds, Proc. SPIE Vol. 5498, Millimeter and Submillimeter Detectors for Astronomy II. SPIE, Bellingham, p. 78

Holland W. S. et al., 1999, MNRAS, 303, 659

Kreysa E. et al., 1998, in Phillips T. G., ed., Proc. SPIE Vol. 3357, Advanced Technology MMW, Radio, and Terahertz Telescopes. SPIE, Bellingham, p. 319

Laurent G. T. et al., 2005, AJ, 623, 742

Mather J. C., 1984, Appl. Opt., 23, 584

Mauskopf P. D., Bock J. J., del Castillo H., Holzapfel W. L., Lange A. E., 1997, Appl. Opt., 36, 765

Scott K.S. et al., 2008, MNRAS, 384, 2225

Souccar K., Wallace G., Malin D., 2004, in Lewis H., Raffi G., eds, Proc. SPIE Vol. 5496, Advanced Software, Control, and Communication Systems for Astronomy. SPIE, Bellingham, p. 241.

Tucker C. E., Ade P. A. R., 2006, in Zmuidzinas J., Holland W. S., Withington S., Duncan W. D., eds, Proc. SPIE Vol. 6275, Millimeter and Submillimeter Detectors and Instrumentation for Astronomy III. SPIE, Bellingham

Turner A. D. et al., 2001, Appl. Opt., 40, 4921

This paper has been typeset from a TEX/LATEX file prepared by the author.